PROCEEDINGS OF SPIE

SPIEDigitalLibrary.org/conference-proceedings-of-spie

# 3D imaging via silicon-photonics-based LIDAR

Remus Nicolaescu, Christopher Rogers, Alexander Piggott, David Thomson, Ion Opris, et al.

Remus Nicolaescu, Christopher Rogers, Alexander Y. Piggott, David J. Thomson, Ion E. Opris, Steven A. Fortune, Andrew J. Compston, Alexander Gondarenko, Fanfan Meng, Xia Chen, Graham T. Reed, "3D imaging via silicon-photonics-based LIDAR," Proc. SPIE 11691, Silicon Photonics XVI, 116910G (5 March 2021); doi: 10.1117/12.2591284

SPIE.

Event: SPIE OPTO, 2021, Online Only

# 3D imaging via silicon-photonics-based LIDAR

Remus Nicolaescu*[a], Christopher Rogers[a], Alexander Y. Piggot[a], David J. Thomson[b], Ion E. Opris[c], Steven A. Fortune[a], Andrew J. Compston[a], Alexander Gondarenko[a], Fanfan Meng[b], Xia Chen[b], Graham T. Reed[b]

[a]Pointcloud, Inc., 329 Bryant St Ste 2D, San Francisco, CA, USA 94107; [b]Optoelectronics Research Centre, University of Southampton, University Road, Southampton, Hampshire, UK SO17 1BJ; [c]Opris Consulting, San Jose, California, USA 95138

## ABSTRACT

Accurate 3D imaging is essential for machines to map and interact with the physical world[1,2]. While numerous 3D imaging technologies exist, each addressing niche applications with varying degrees of success, none have achieved the breadth of applicability and impact that digital image sensors have achieved in the 2D imaging world[3-10]. A large-scale two-dimensional array of coherent detector pixels operating as a light detection and ranging (LIDAR) system could serve as a universal 3D imaging platform. Such a system would other high depth accuracy and immunity to interference from sunlight, as well as the ability to directly measure the velocity of moving objects[11]. However, due to difficulties in providing electrical and photonic connections to every pixel, previous systems have been restricted to fewer than 20 pixels[12-15]. Here, we demonstrate the first large-scale coherent detector array consisting of 512 (32×16) pixels, and its operation in a 3D imaging system. Leveraging recent advances in the monolithic integration of photonic and electronic circuits, a dense array of optical heterodyne detectors is combined with an integrated electronic readout architecture, enabling straightforward scaling to arbitrarily large arrays. Meanwhile, two-axis solid-state beam steering eliminates any tradeoff between field of view and range. Operating at the quantum noise limit[16,17], our system achieves an accuracy of 3.1 mm at a distance of 75 meters using only 4 mW of light, an order of magnitude more accurate than existing solid-state systems at such ranges. Future reductions of pixel size using state-of-the-art components could yield resolutions in excess of 20 megapixels for arrays the size of a consumer camera sensor. This result paves the way for the development and proliferation of low cost, compact, and high-performance 3D imaging cameras, enabling new applications from robotics and autonomous navigation to augmented reality and healthcare.

**Keywords:** 3D imaging, light detection and ranging (LIDAR), silicon photonics, focal plane array (FPA), frequency modulated continuous wave (FMCW)

## 1. INTRODUCTION

The digital complementary metal-oxide-semiconductor (CMOS) image sensor, borrowing technology from silicon micro-electronics to produce a flexible and scalable camera sensor, revolutionized 2D imaging[18]. As a focal plane array (FPA), the digital image sensor operates in concert with a lens that focuses light and forms an image on the detector. A key advantage of this scheme is that the field of view and light collection efficiency are not set by the image sensor, but instead by the choice of lens. Furthermore, the CMOS image sensor can be optimized for high performance or cost, allowing it to be fine-tuned for different applications. Due to the great flexibility afforded by this arrangement, the digital CMOS sensor has become the sensor of choice for the majority of 2D imaging.

In contrast, the world of 3D imaging is characterized by a vast assortment of competing technologies, each addressing a small niche of applications. Long range and high precision applications such as autonomous vehicles and construction site mapping are dominated by expensive and fragile mechanically steered light detection and ranging (LIDAR) systems[3,4]. Meanwhile, solid-state solutions such as structured light[5] and time-of-flight arrays[6-10,19,20] are used when affordability, compactness, and reliability must be achieved at the expense of performance, such as in mobile devices and augmented reality systems. Optical phased arrays are a promising solid-state approach, but the development of long-range 2D-scanning systems has proved challenging, with current demonstrations limited to less than 20 meters[21-23]. As such, no currently available technology can address the needs of these diverse use cases.

*remus.nicolaescu@point.cloud; phone 1 415 297-3301; http://point.cloud

Silicon Photonics XVI, edited by Graham T. Reed, Andrew P. Knights, Proc. of SPIE Vol. 11691, 116910G · © 2021 SPIE · CCC code: 0277-786X/21/$21 · doi: 10.1117/12.2591284

Pointcloud, Inc. has developed a fully solid-state, integrated photonic LIDAR based on the same FPA concept as the CMOS image sensor. By making efficient use of light, our system achieves the long range and high depth accuracy needed for demanding applications such as self-driving vehicles[1] and drone-based 3D mapping[24,25]. The architecture also scales to arbitrarily large fields of view. The centerpiece of our system is the coherent receiver array, an extremely sensitive array of compact optical heterodyne detectors operating at the quantum noise limit[16,17]. To eliminate any tradeoff between field of view and range, the receiver is paired with a solid-state beam steering mechanism that sequentially illuminates the target scene in small patches. While previous demonstrations of this concept have been limited to fewer than 20 pixels due to the reliance on direct electrical connections to each pixel[12-15], our initial prototype array contains 512 pixels and can be scaled to arbitrarily large numbers of pixels by simply increasing the size of the array. Furthermore, our use of a standard process provided by a commercial foundry allows our system to be immediately mass produced for minimal cost.

## 2. SCALABLE 3D IMAGING ARCHITECTURES

Our LIDAR system is built around one of two different types of pixels comprising a receiver FPA: a bistatic architecture that relies on two separate focal plane arrays, one acting as a transmitter and one as a receiver, with corresponding separate optical paths, and a monostatic architecture that instead combines the transmit and receive paths within each pixel using a 2×2 50/50 directional coupler. In both architectures, scattered light from the scene is collected by a grating coupler and mixed with the LO light on a balanced detector consisting of a 50/50 directional coupler and germanium PIN photodiodes, producing a heterodyne tone corresponding to the target's distance.

The coherent receiver array allows our architecture to operate using the robust frequency-modulated continuous-wave (FMCW) coherent LIDAR scheme[26,27]. In contrast to widely used time-of-flight LIDARs that rely on transmitting short pulses of light, an FMCW LIDAR uses a linearly chirped laser as both the transmit beam and the local oscillator. Scattered light received from the target is mixed with the local oscillator light in a heterodyne receiver, producing a beat frequency proportional to the round-trip travel time, and hence the distance to the target.

The FMCW scheme confers our architectures with several key advantages relative to time-of-flight schemes. First, due to the use of heterodyne detection, the system is immune to interference from sunlight and other LIDAR systems operating nearby since it selectively detects light close in frequency to the local oscillator light[11]. Second, a coherent LIDAR can directly measure the velocity of moving objects by sensing the Doppler shift of the received signal[26,27]. Third, high depth accuracy only depends upon the chirp bandwidth and signal-to-noise ratio[28], thus allowing the receiver electronics to operate at relatively low frequencies, in contrast with time-of-flight schemes where depth accuracy is limited by receiver bandwidth. Finally, the FMCW system is well suited for integrated photonic LIDARs, which are constrained in peak power due to nonlinear effects[29,30]. Whereas time-of-flight schemes emit photons in short, high-power bursts, the FMCW scheme emits photons continuously and maximizes the number of emitted photons, thereby improving the system's range.

We implemented our LIDAR system on GlobalFoundries's CMS90WG process, a silicon photonics process with monolithically integrated CMOS electronics. This technology allowed us to incorporate a highly multiplexed electronic readout architecture directly into the receiver array, minimizing the number of required external electrical connections while maintaining signal integrity.

### 2.1 Coherent focal plane array – bistatic implementation

A single pixel of the bistatic receiver is schematically shown in Figure 1(a). Each pixel collects scattered light from the scene using a grating coupler. Local oscillator (LO) light is provided to each pixel via a network of silicon waveguides. Scattered and LO light are mixed on a balanced detector consisting of a 50/50 directional coupler and germanium PIN photodiodes, producing a heterodyne tone corresponding to the target's distance. The signal is then amplified by a transimpedance amplifier (TIA) integrated within the pixel.

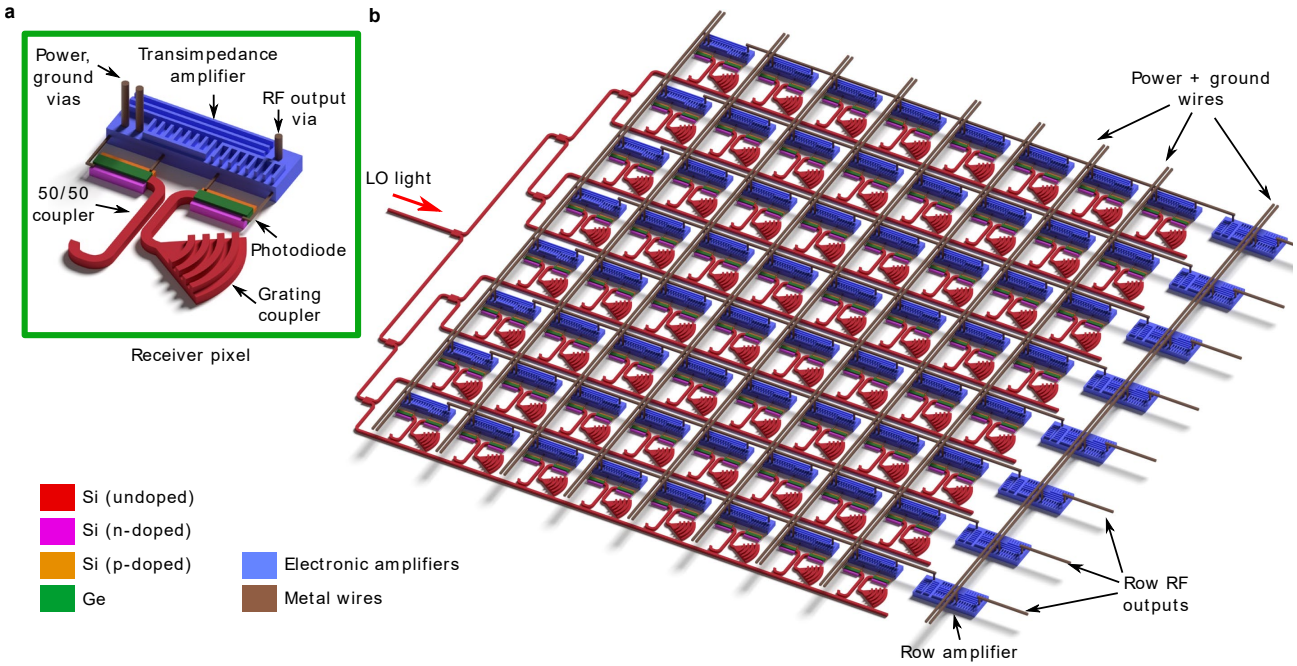


Figure 1. Receiver focal plane array (FPA) design. (a) Schematic of a single receiver pixel consisting of a grating coupler that receives scattered light, a 50/50 coupler and pair of photodiodes that mix incoming scattered light with LO light, and an integrated transimpedance amplifier (TIA). (b) An 8x8 block or our receiver FPA showing the distribution of LO light through a network of silicon waveguides and the additional electronic amplification stages at the end of each row.

Monolithic integration of the electronics into the receiver FPA facilitates the use of an actively multiplexed readout architecture, allowing the receiver to be scaled to arbitrarily large number of pixels. A buffer amplifier is shared among the pixels of each row and maintains wide bandwidth while driving the large parasitic capacitances of the wiring and multiplexed circuitry, which is demonstrated in Figure 1(b). Simultaneously, active driver amplifiers carry the signal to the edge of the chip, enabling parallel readout. In our first demonstrator chip, multiple levels of multiplexing and amplification were used to map 32×16 pixels to 8 outputs while maintaining signal integrity.

### 2.2 Full system architecture – bistatic implementation

As shown in Figure 2, the bistatic architecture utilizes two FPAs. The first acts as a transmitter, and the second acts as a receiver. Chirped laser light for the FMCW scheme is generated external to the chip by modulating a fixed-frequency 1550 nm laser with a silicon-photonic in-phase/quadrature (IQ) Mach-Zehnder modulator (MZM), which is in turn driven by an arbitrary waveform generator. This approach ensures chirp linearity and enables the use of a simple, low-noise laser.

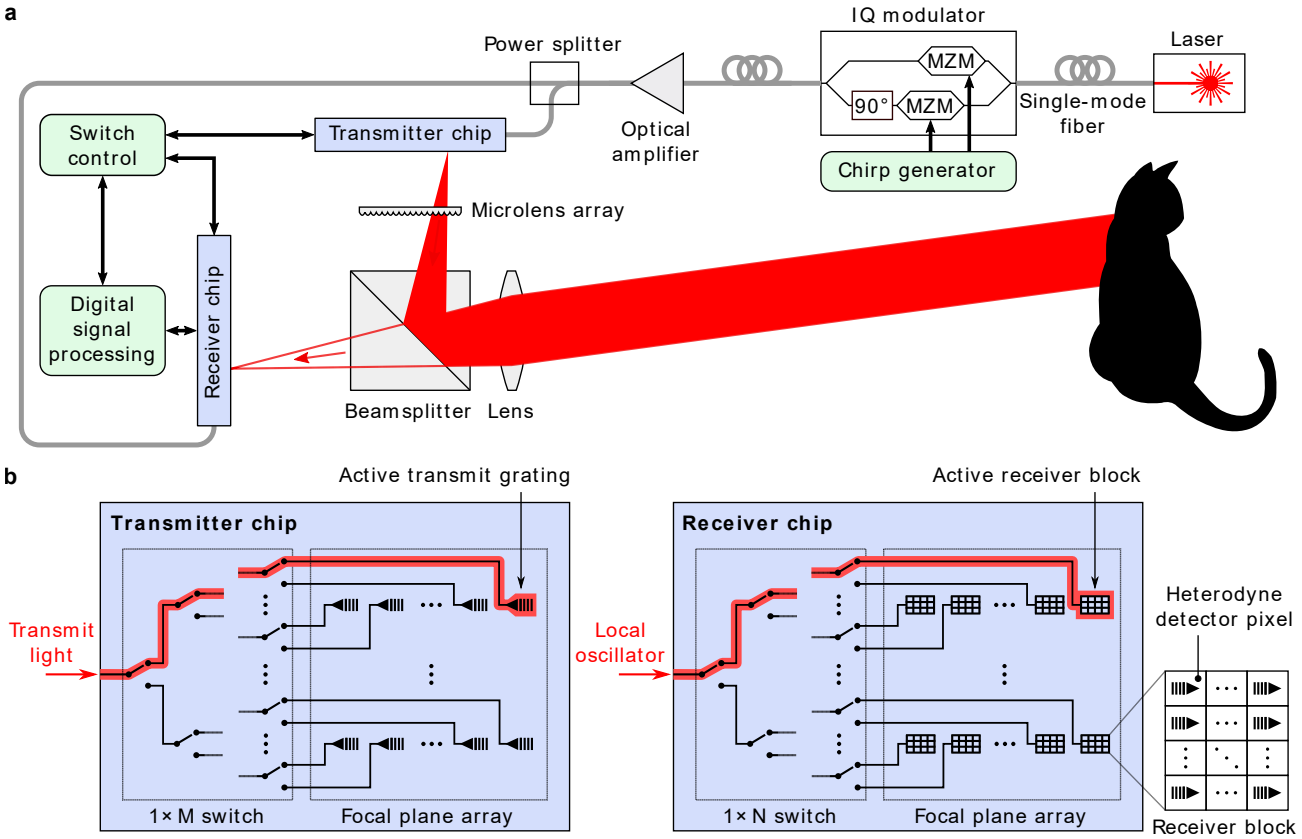


Figure 2. Solid-state 3D imaging architecture. (a) Our architecture consists of two focal plane arrays (FPAs): a transmitter FPA that sequentially illuminates patches of the scene, and a receiver FPA that detects scattered light from the scene. The frequency-modulated continuous-wave (FMCW) scheme is used for ranging. An optional microlens array can be used to shape the illumination pattern to more closely match the receiver array, thereby improving system efficiency. (b) On-chip steering of light is provided by thermo-optic switching trees on both the transmitter and receiver chips.

Long-range performance is achieved by sequentially illuminating and reading out the scene in small patches, thereby allowing us to use light as efficiently as possible. This guiding of light is accomplished on the transmitter side by a switching tree terminated by a FPA of grating couplers. Light is directed to one transmit grating at a time, illuminating a small subset of the scene. This switching approach to beam steering is robust and can be scaled up to arbitrarily large arrays with optical losses limited only by waveguide scattering[31] and the extinction ratio of the switching trees. Meanwhile, the receiver consists of a dense FPA of miniaturized heterodyne receivers. All receiver pixels that correspond to the illuminated area are simultaneously read out in parallel. Since the angular resolution is defined by the point spread function of the lens, which drops off very quickly, there is negligible crosstalk between different receiver pixels. Additionally, to avoid wasting LO light, a second switching tree is used to provide only the activated subset of the receiver FPA with LO light.

The use of parallel readout in the receiver is fundamental to the scalability of our architecture. First, the system resolution is defined by the number of pixels in the receiver FPA rather than the number of steering positions, which significantly improves the system resolution for a given chip size since heterodyne receiver pixels are roughly an order of magnitude smaller than thermo-optic switches. Second, parallel readout eliminates the need for fast thermo-optic switching because the number of measured points per second is decoupled from the switching rate. Finally, due to the use of an FMCW scheme, parallel readout proportionally reduces the receiver signal frequencies by allowing longer ramp times, simplifying the readout electronics.

### 2.3 Monostatic pixel architecture

An alternative system and pixel architecture combines the transmit and receive paths within each pixel using a 2×2 50/50 directional coupler. A single pixel is schematically shown in Figure 3. Each pixel acts as both a transmitter and a receiver

with the outbound signal being directed by two grating couplers out of the plane of the chip and towards the scene. The same two grating couplers are used to collect scattered light from the scene. LO light is provided to each pixel via a network of silicon waveguides. Scattered and LO light are mixed on a balanced detector consisting of a 50/50 directional coupler and germanium PIN photodiodes, producing a heterodyne tone corresponding to the target's distance. The signal is then amplified by a TIA integrated within the pixel. While in this configuration a 3 dB loss is incurred as half the return light is directed towards the signal bus and lost, the architecture has the advantage of not requiring the alignment of a receiver FPA to a transmitter FPA and requires only one lens system for imaging, hence vastly simplifying the system assembly and number of components.

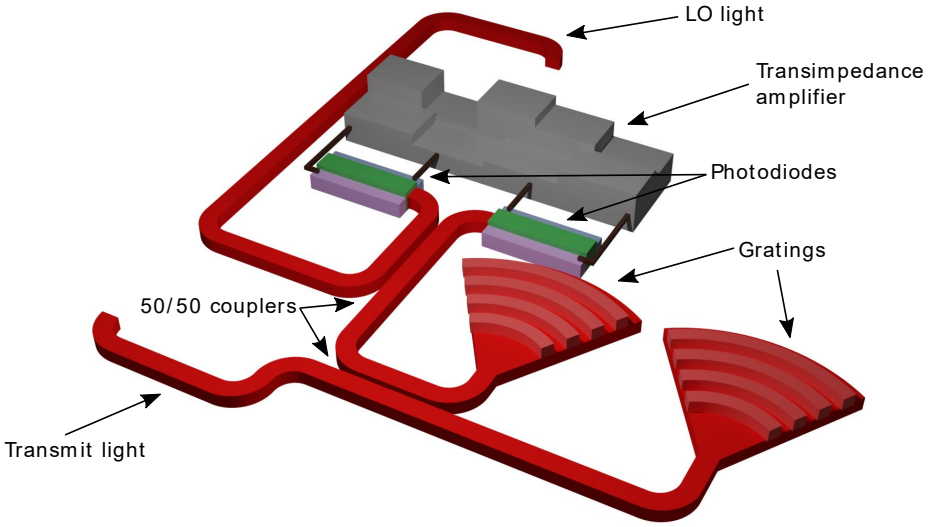


Figure 3. Schematic of a single pixel of the monostatic architecture. In contrast with the bistatic pixel, which acts only as a receiver, this pixel combines the transmit and receive paths within the pixel. It uses two gratings to send and collect the signal and a similar balanced detection scheme that mixes the received scattered light with the LO light on detectors followed by an integrated transimpedance amplifier.

### 2.4 Full system architecture – monostatic implementation

As shown in Figure 4, the monostatic system architecture is based on just a single FPA. As in the bistatic full system architecture, chirped laser light for the FMCW scheme is generated external to the chip by modulating a fixed-frequency 1550 nm laser with a silicon-photonic IQ MZM, which is in turn driven by an arbitrary waveform generator. This approach ensures chirp linearity and enables the use of a simple, low-noise laser. The transmit and the LO switching trees are synchronized so that active pixels are simultaneously supplied with both transmit light and LO light.

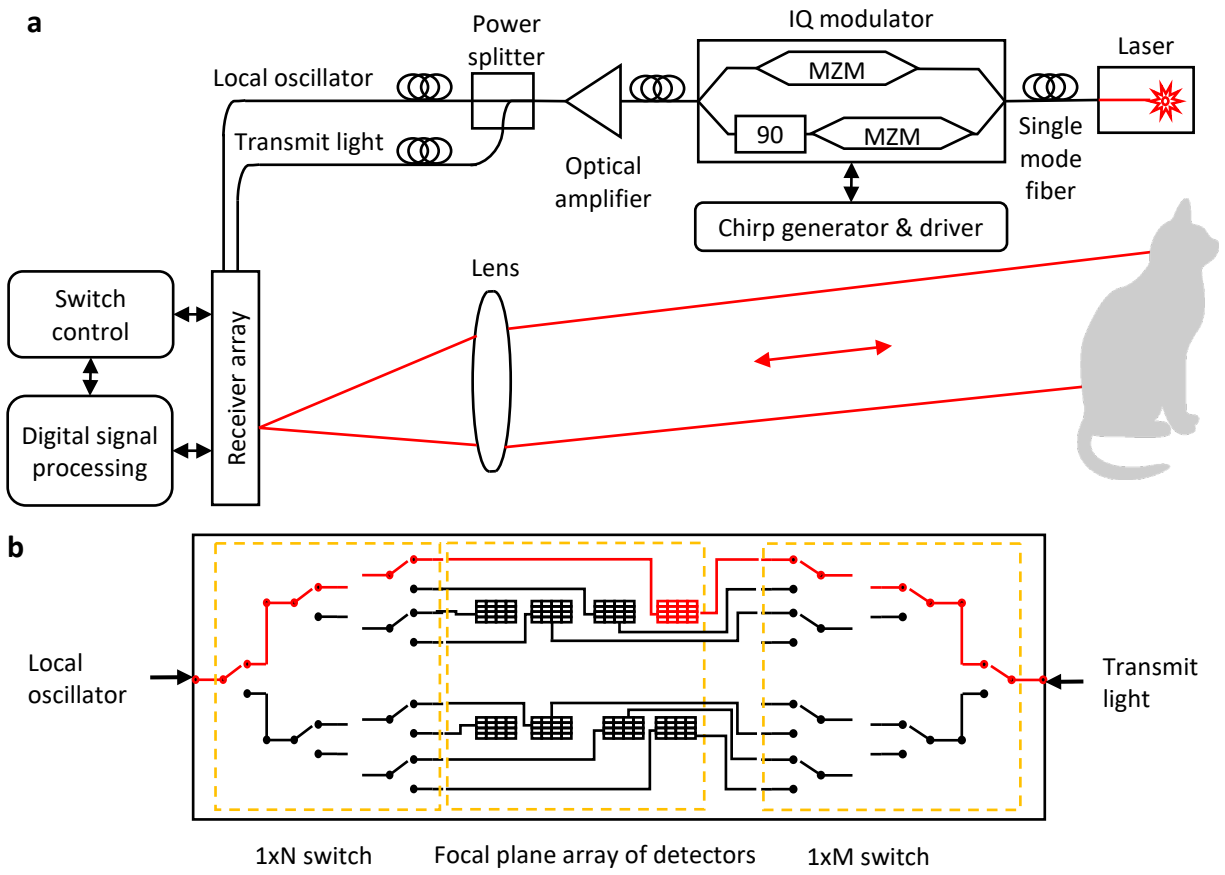


Figure 4. Monostatic system architecture. (a) A single FPA receiver with the same chirp generator as with the bistatic system. (b) On-chip steering of light is similarly controlled by two thermo-optic switching trees but the same chip.

The same TIA and parallel readout structure are utilized in this architecture as well as for the bistatic implementation. As such, this architecture also scales in a similar manner. Our first chip demonstrating the monostatic pixel architecture consists of 16×16 pixels mapped to 8 simultaneous outputs.

## 3. RESULTS

Point clouds of a rotating basketball at 17 m, stacked boxes at 55 m, and an exterior wall from our bistatic LIDAR system first prototype chip are illustrated in Figure 5. Our 3D imager was operated with an emitter power of only 4 mW at the aperture, a chirp bandwidth of 4 GHz, and up- and down-chirp lengths of 850 µs. The point clouds were generated by stacking 3 sequential frames to minimize the number of missing pixels due to speckle effects, which equally impacts all coherent RADAR and LIDAR schemes[32]. No incoherent averaging was used.

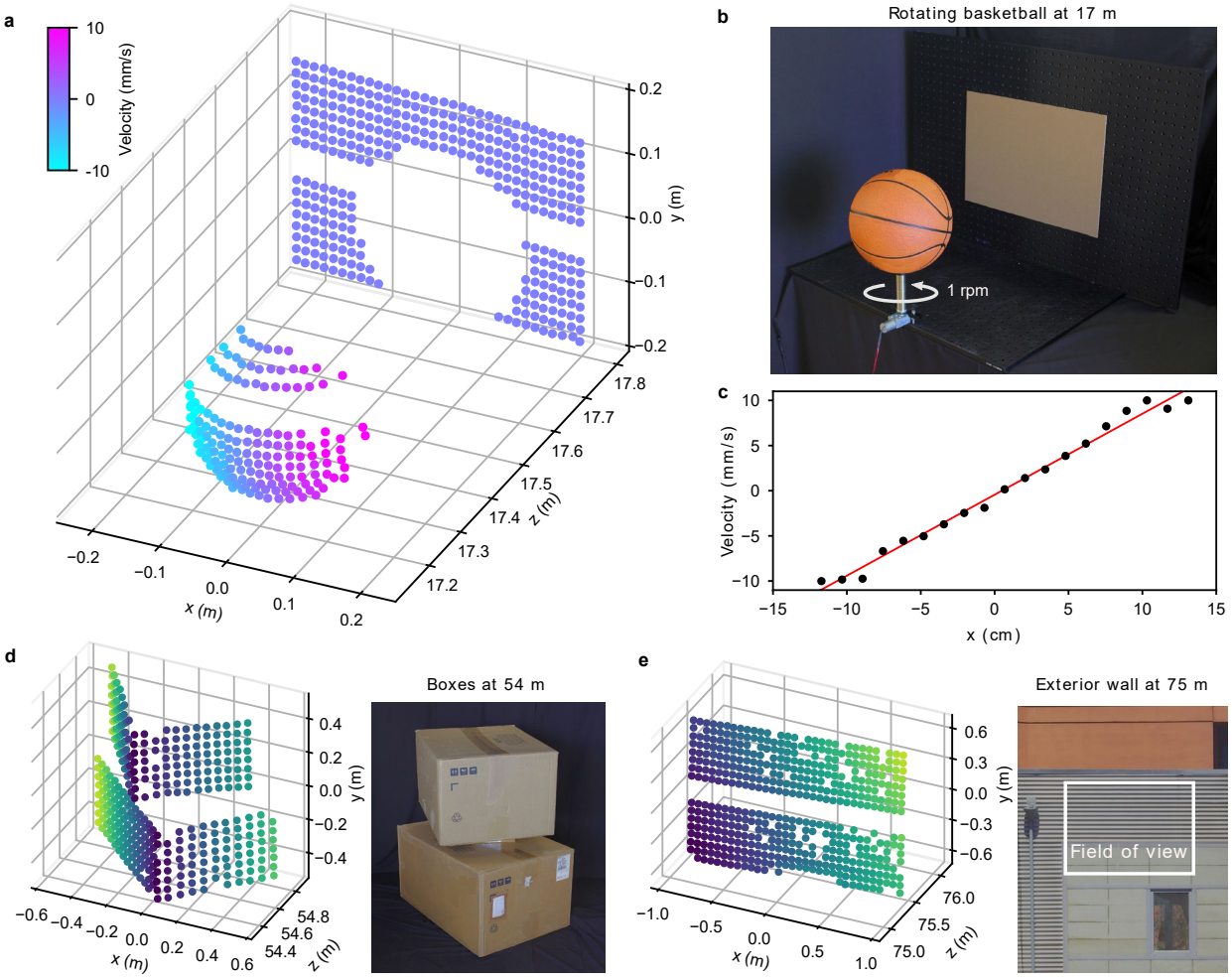


Figure 5. Point clouds from 3D imaging system. (a) Velocity annotated point cloud of a basketball at 17 m rotating about its vertical axis at 1 rpm. (b) Photograph of the basketball setup. (c) Horizontal linecut of velocity across the middle of the basketball. (d, e) Point clouds of (d) stacked cardboard boxes at 54 m, and (e) an exterior wall at 75 m. Distance to the target is indicated by color in (d) and (e).

We further demonstrate the performance of our system in Figure 6. By placing a retroreflector in the system's field of view, we measured >25 dB contrast for a 1-pixel displacement and >50 dB contrast for a 4-pixel displacement, with further displacements reaching the system noise floor, illustrating the excellent pixel-to-pixel isolation in our system. Additionally, our system has a depth precision of less than 3 mm for distances out to as high as 60 m, and the precision and detection probability improve for closer ranges.

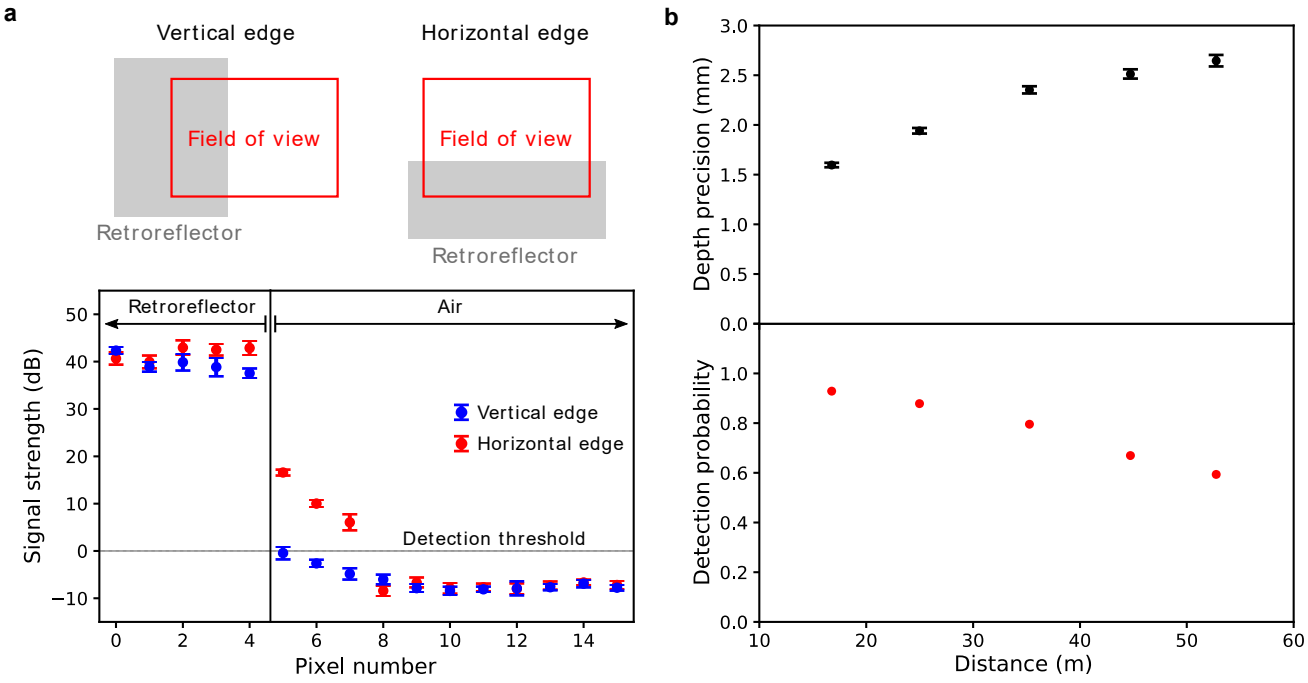


Figure 6. Characterization of system performance. (a) Imaging contrast measured using retroreflective sheeting. Here, the error bars represent the standard error. (b) Depth precision and detection probability as a function of distance for a 44% reflectance target. The error bars on the depth precision represent the 95% confidence intervals.

Demonstration of our first monostatic LIDAR system prototype chip is presented in Figure 7. This 3D imager was operated with an emitter power of only 1 mW at the aperture, a chirp bandwidth of 4 GHz, and up- and down-chirp lengths of 20 µs. A point cloud of a football at 14 m, is illustrated in Fig. 7(a). The point cloud was generated in one frame and shows probability of detection in excess of 90%. No incoherent averaging was used. In the monostatic array 8 pixels are illuminated and read simultaneously. The energy per point for the 14 m measurement is 2.5 nJ.

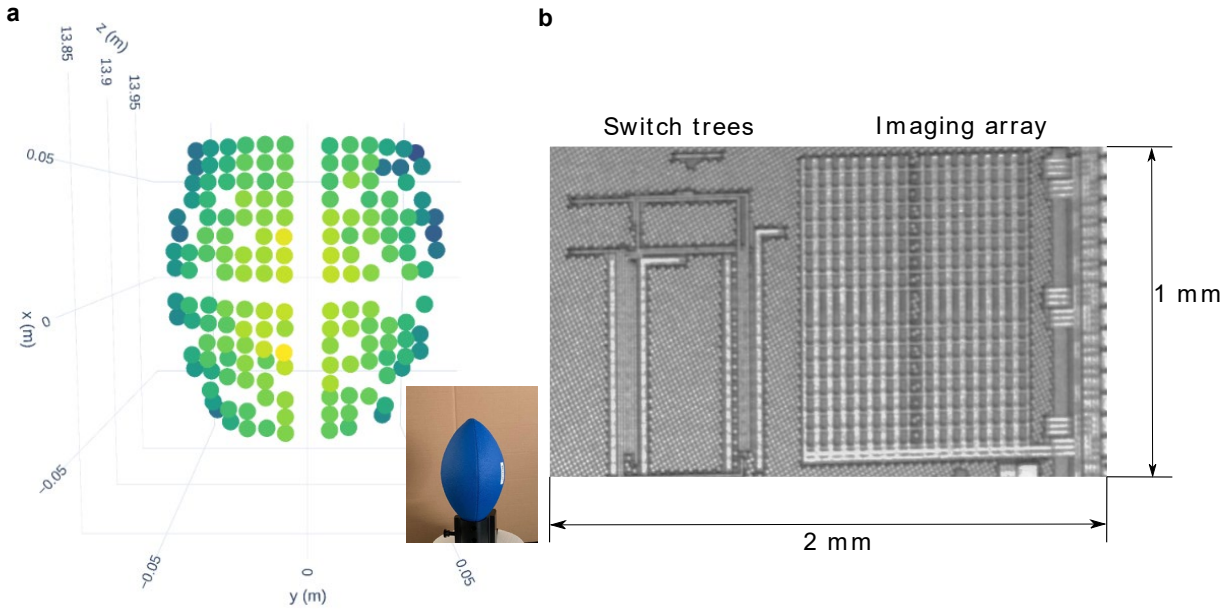


Figure 7. Monostatic 3D imaging system using a 16×16 pixels array. (a) Point cloud of a football at 14 m using a total emitter power of 1 mW a chirp bandwidth of 4 GHz, and up- and down-chirp lengths of 20 µs. (b) micrograph of the chip showing a 0.92 mm$^2$ monostatic FPA using pixels with pixel size of 63 µm × 57 µm.

# 4. DISCUSSION AND OUTLOOK

We have demonstrated a scalable solid-state 3D imaging architecture that achieves >70 m range and millimeter-class accuracy, all while using only 4 mW of transmitted power. Our 3.1 mm precision is an order of magnitude higher than existing solid-state 3D imagers at these ranges, with state-of-the-art flash LIDAR systems limited to an accuracy of several centimeters for distances greater than 50 meters[7-10]. Furthermore, this level of performance meets the needs of a variety of demanding applications that were previously out of reach for solid-state 3D imaging systems. For example, self-driving vehicles need a LIDAR that uses low levels of laser energy to remain eye safe yet still have the ability to reach long ranges with high accuracy[1]. Currently, this combination of requirements is typically met using mechanically steered LIDARs, such as the commonly used Velodyne VLP-16. This 100 m class mechanical LIDAR uses the same 0.2 μJ of light per point as our system[4] but has a much poorer depth accuracy of 3 cm. Meanwhile, the 3D mapping of buildings and construction sites using drones[24,25] and stationary scanners[2] requires millimeter-class accuracy at distances of tens of meters[33], which is easily achieved by our system. Finally, our system's ability to measure velocity with high accuracy enables preventive healthcare applications such as remote vital signs monitoring by measuring the movement of a patient's chest.

## 4.1 Scaling of system

Our 3D imaging architecture naturally scales to large arrays. By using a $1 \times N$ switching tree to steer light, the number of active thermo-optic switches and associated DACs and drivers needed for control scales as $O(\log N)$. On the receiver side, power consumption depends only upon the number of parallel readout channels rather than the size of the full array since only active amplifiers are powered at any given time. The fundamental limit on array size therefore comes from the size of the chip. At our current receiver pixel pitch of 80×100 μm$^2$, chips the size of a full-frame camera sensor (36×24 mm$^2$) would have QVGA (320×240 pixel) resolution. However, using state-of-the-art designs, 8×5 μm$^2$ are feasible, corresponding to full-frame sensors with resolutions of 4500×4800 pixels.

Multiple options exist to reduce the pixel size: a) reduction of the optical components size though design optimization b) shifting the wavelength of operation towards 1300 nm leading to inherent optical component shrink c) optimization of SOI thickness to allow for optimal ratio between active switching vs passive splitting within the FPA and reduction of the number of switches and d) use of a backside illuminated architecture. In a backside illuminated architecture the backside of the wafer is polished and coated with an antireflection coating while a metal layer is used as a reflector to direct the light emitted by the grating couplers to exit through the backside. This enables the use of a wafer bonding process in which the silicon photonics wafer is bonded with a separate wafer on which the electronics resides. By moving the sensor electronics onto a separate wafer, we allow for a significant reduction in pixel size as the TIAs and electrical routing can move from a side by side to a stacked configuration and similarly for the switch optical and electrical components. Pointcloud and the University of Southampton teams are actively working on a backside-illuminated architecture as illustrated in Figure 8 and a switch has already been successfully demonstrated.

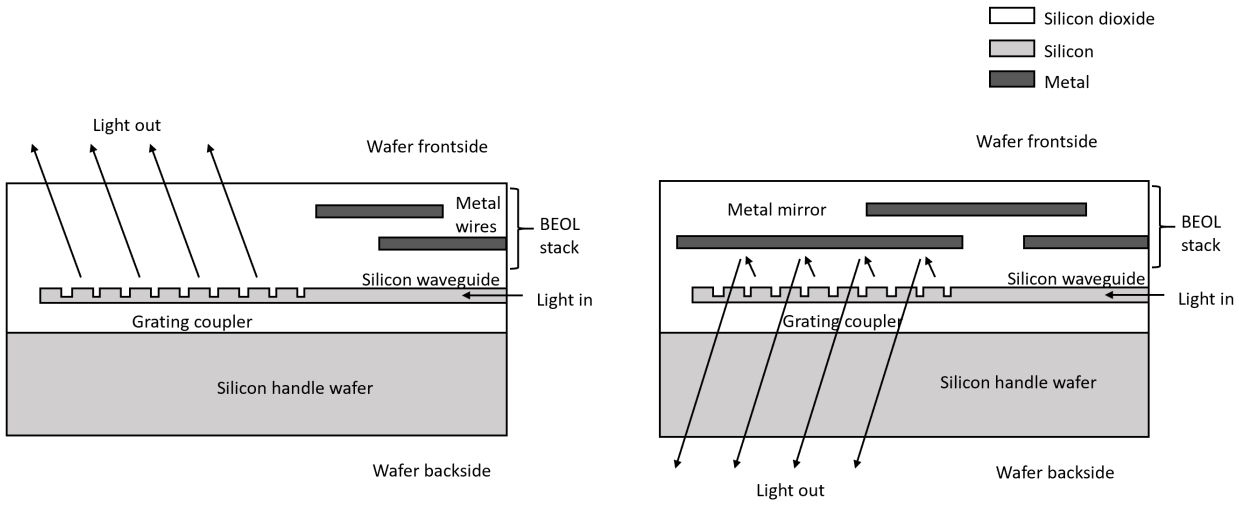


Figure 8. Backside vs frontside illuminated imager configurations. In a backside illuminated configuration a metal layer is used to create a reflector and direct the light emitted by the grating through the backside of the wafer.

### 4.2 Conclusions

We have developed a universal solid-state 3D imaging architecture that has the potential to meet the needs of nearly all 3D imaging applications, spanning from robotics, autonomous navigation, and biomedical devices to consumer products such as augmented reality headsets. Our results suggest that the equivalent of the CMOS image sensor for 3D imaging is imminent, ushering in a broad range of applications which were previously impractical or unimaginable.

## REFERENCES

[1] Urmson, C., Anhalt, J., Bagnell, D., Baker, C., Bitner, R., Clark, M. N., Dolan, J., Duggins, D., Galatali, T., Geyer, C., Gittleman, M., Harbaugh, S., Hebert, M., Howard, T. M., Kolski, S., Kelly, A., Likhachev, M., McNaughton, M., Miller, N., Peterson, K., Pilnick, B., Rajkumar, R., Rybski, P., Salesky, B., Seo, Y.-W., Singh, S., Snider, J., Stentz, A., Whittaker, W. R., Wolkowicki, Z., Ziglar, J., Bae, H., Brown, T., Demitrish, D., Litkouhi, B., Nickolaou, J., Sadekar, V., Zhang, W., Struble, J., Taylor, M., Darms, M. and Ferguson, D, "Autonomous driving in urban environments: Boss and the Urban Challenge," Journal of Field Robotics 25, 425-466 (2008).

[2] Wang, Q. and Kim, M.-K., "Applications of 3D point cloud data in the construction industry: A fifteen-year review from 2004 to 2018," Advanced Engineering Informatics 39, 306-319 (2019).

[3] Lichti, D. D. "Error modlling, calibration and analysis of an AM-CW terrestrial laser scanner system," ISPRS Journal of Photogrammetry and Remote Sensing 61, 307-324 (2007).

[4] Kidd, J. "Performance evaluation of the velodyne VLP-16 system for surface feature surveying," Master's thesis, University of New Hampshire (2017), <https://scholars.unh.edu/thesis/1116>.

[5] Salvi, J., Pagès, J. and Batlle, J., "Pattern codification strategies in structured light systems," Pattern Recognition 37, 827-249 (2004).

[6] Corti, A., Giancola, S., Mainetti, G. and Sala, R., "A metrological characterization of the Kinect V2 time-of-flight camera," Robotics and Autonomous Systems 75, 584-594 (2016).

[7] McManamon, P., "Review of LADAR: a historic, yet emerging, sensor technology with rich phenomenology," Optical Engineering 51, 1-14 (2012).

[8] McManamon, P F., Banks, P. S., Beck, J. D., Fried, D. G., Huntington, A. S. and Watson, E. A., "Comparison of flash LiDAR detector options," Optical Engineering 56, 1-23 (2017).

[9] Hutchings, S. W., Johnston, N., Gyongy, I., Al Abbas, T., Dutton, N. A. W., Tyler, M., Chan, S., Leach, J. and Henderson, R. K., "A reconfigurable 3-D-stacked SPAD imager with in-pixel histogramming for flash LIDAR or high-speed time-of-flight imaging," IEEE Journal of Solid-State Circuits 54, 2947 (2019).

[10] Ronchini Ximenes, A., Padmanabhan, P., Lee, M., Yamashita, Y., Yaung, D. and Charbon, E., "A modular, direct time-of-flight depth sensor in 45/65-nm 3-D-stacked CMOS technology," IEEE Journal of Solid-State Circuits 54, 3203 (2019).
[11] Behroozpour, B., Sandborn, P. A. M., Wu, M. C. and Boser, B. E., "Lidar system architectures and circuits," IEEE Communications Magazine 55, 135-142 (2017).
[12] Aflatouni, F., Abiri, B., Rekhi, A. and Hajimiri, A., "Nanophotonic coherent imager," Opt. Express 23, 5117-5125 (2015).
[13] Martin, A., Dodane, D., Leviandier, L., Dolfi, D., Naughton, A., O'Brien, P., Spuessens, T., Baets, R., Lepage, G., Verheyen, P., De Heyn, P., Absil, P., Feneyrou, P. and Bourderionnet, J., "Photonic integrated circuit-based FMCWcoherent LiDAR," Journal of Lightwave Technology 36, 4640-4645 (2018).
[14] Inoue, D., Ichikawa, T., Kawasaki, A. and Yamashita, T., "Demonstration of a new optical scanner using silicon photonics integrated circuit," Opt. Express 27, 2499-2508 (2019).
[15] Li, C., Cao, X., Wu, K., Li, X. and Chen, J., "Lens-based integrated 2d beam-steering device with defocusing approach and broadband pulse operation for lidar application," Opt. Express 27, 32970-32983 (2019).
[16] Collett, M., Loudon, R. and Gardiner, C., "Quantum theory of optical homodyne and heterodyne detection," Journal of Modern Optics 34, 881-902 (1987).
[17] Rubin, M. A. and Kaushik, S., "Squeezing the local oscillator does not improve signal-to-noise ratio in heterodyne laser radar," Opt. Lett. 32, 1369-1371 (2007).
[18] El Gamal, A. and Eltoukhy, H., "CMOS image sensors," IEEE Circuits and Devices Magazine 21, 6-20 (2005).
[19] Stann, B. L., Aliberti, K., Carothers, D., Dammann, J., Dang, G., Giza, M. M., Lawler, W. B., Redman, B. C. and Simon, D. R., "A 32x32 pixel focal plane array ladar system using chirped amplitude modulation," Proc. SPIE 5412, 264-272 (2004).
[20] Hu, K., Zhao, Y., Ye, M., Gao, J., Zhao, G. and Zhou, G., "Design of a CMOS ROIC for InGaAs self-mixing detectors used in FM/cw LADAR," IEEE Sensors Journal 17, 5547-5557 (2017).
[21] Poulton, C. V., Yaacobi, A., Cole, D. B., Byrd, M. J., Raval, M., Vermeulen, D. and Watts, M. R., "Coherent solid-state LIDAR with silicon photonic optical phased arrays," Opt. Lett. 42, 4091-4094 (2017).
[22] Miller, S. A., Phare, C. T., Chang, Y.-C., Ji, X., Gordillo, O. A. J., Mohanty, A., Roberts, S. P., Shin, M. C., Stern, B., Zadka, M. and Lipson, M., "512-element actively steered silicon phased array for low-power LIDAR," Proc. OSA JTh5C.2, 2018.
[23] Poulton, C. V., Byrd, M. J., Russo, P., Timurdogan, E., Khandaker, M., Vermeulen, D. and Watts, M. R., "Long-range LiDAR and free-space data communication with high-performance optical phased arrays," IEEE Journal of Selected Topics in Quantum Electronics 25, 1-8 (2019).
[24] Wang, J., Sun, W., Shou, W., Wang, X., Wu, C., Chong, H.-Y., Liu, Y. and Sun, C., "Integrating BIM and LiDAR for real-time construction quality control," Journal of Intelligent & Robotic Systems 79, 417-432 (2015).
[25] Kasturi, A., Milanovic, V., Atwood, B. H. and Yang, J., "UAV-borne lidar with MEMS mirror-based scanning capability," Proc. SPIE 9832, 206-215 (2016).
[26] Griffiths, H. D., "New ideas in FM radar," Electronics Communication Engineering Journal 2, 185-194 (1990).
[27] Riemensberger, J., Lukashchuk, A., Karpov, M., Weng, W., Lucas, E., Liu, J. and Kippenberg, T. J., "Massively parallel coherent laser ranging using a soliton microcomb," Nature 581, 164-170 (2020).
[28] Thurn, K., Ebelt, R. and Vossiek, M., "Noise in homodyne FMCW radar systems and its effects on ranging precision," Proc. IEEE MTT-S International Microwave Symposium, 1-3 (2013).
[29] Tsang, H. K., Wong, C. S., Liang, T. K., Day, I. E., Roberts, S. W., Harpin, A., Drake, J. and Asghari, M., "Optical dispersion, two-photon absorption and self-phase modulation in silicon waveguides at 1.5 μm wavelength," Applied Physics Letters 80, 416-418 (2002).
[30] Rong, H., Liu, A., Jones, R., Cohen, O., Hak, D., Nicolaescu, R., Fang, A. and Paniccia, M., "An all-silicon Raman laser," Nature 433, 292–294 (2005).
[31] Shen, Y., Harris, N. C., Skirlo, S., Prabhu, M., Baehr-Jones, T., Hochberg, M., Sun, X., Zhao, S., Larochelle, H., Englund, D. and Soljačić, M., "Deep learning with coherent nanophotonic circuits," Nature Photonics 11, 441-446 (2017).
[32] Wang, J. Y. "Heterodyne laser radar-SNR from a diffuse target containing multiple glints," Appl. Opt. 21, 464-476 (1982).
[33] Rebolj, D., Pučko, Z., Babič, N. Čuš., Bizjak, M., and Mongus, D., "Point cloud quality requirements for scan-vs-BIM based automated construction progress monitoring," Automation in Construction 84, 323-334 (2017).